Design and Analysis of Alternative Structural Concepts for the Orion Heat Shield Carrier Structure

James J. Ainsworth[1], Eric A. Gustafson[2], Craig S. Collier[1]
[1]Collier Research Corp.
760 Pilot House Dr.
Newport News, VA 23606
[2]Structural Design and Analysis, Inc. (SDA)
46030 Manekin Plaza Ste. 120
Sterling, VA 20166

1. ABSTRACT

During a two year contract, Collier Research Corp. and SDA worked side-by-side with the NASA Engineering and Safety Center and Lockheed Martin Space Systems to design an alternate concept for the heat shield carrier structure for the Orion Multi-Purpose Crew Vehicle. The heat shield carrier structure must hold the 5-meter diameter thermal protection system securely to the Orion spacecraft. Several structural concepts were investigated, including designs that incorporated load sharing with the crew module backbone, replacing the existing wagon wheel stringer design with an H beam configuration, and switching the composite Carbon/Cyanate Ester skin to Titanium material and orthogrid stiffening concept. Analytical methods were developed to evaluate the strength and stability of the heat shield carrier structure for launch and reentry loads, greater than 2923 K (2,650 °C) reentry temperatures, and dynamic splash down impact events. Transient nonlinear landing simulations were run in LS-DYNA to capture the load introduction. These simulations introduced the complete vehicle to a water pool at various speeds and orientations. The dynamic FEA results were imported into HyperSizer and automated closed-form analysis methods were used for detailed sizing and margin of safety reports. This paper outlines the design and analysis process and reviews the analytical methods used to perform the trade studies of the Orion heat shield carrier structure. The analysis methods have been verified with nonlinear FEA and validated with dynamic impact testing.

2. INTRODUCTION

In 2012, an independent technical assessment team with the NASA Engineering and Safety Center's (NESC) was tasked with designing an alternative structural concept for the Orion Heat Shield Carrier (HSC) structure. The team concluded that a titanium orthogrid design for the carrier structure could reduce the overall system mass by more than 363 kg (800 lb) (approximately 25%). During the two year contract, Collier Research and SDA developed analytical methods for the structural analysis of the alternate HSC structure. The primary objective was to develop an automated sizing process for the HSC structure that included analytical methods required to assess the strength and stability of a reentry vehicle heat shield that is subject to harsh reentry and water landing environments.

2.1 Orion Multi-Purpose Crew Vehicle

Figure 1 illustrates the Orion Multi-Purpose Crew Vehicle (MPCV). This manned spacecraft is being built by Lockheed Martin Space Systems (LMSS) for beyond low Earth orbit crewed missions to asteroids, and with the potential for deep space missions to Mars. The vehicle is planned to be launched into orbit by the Space Launch Systems (SLS) launch vehicle.

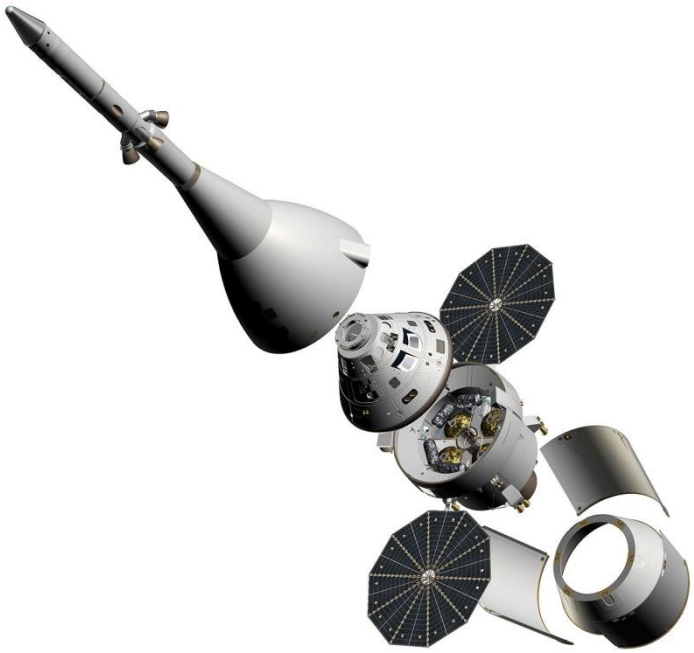

Figure 1. MPCV assembly. (Top to bottom) Launch Abort System (LAS), Crew Module (CM), Service Module (SM) and Spacecraft Adapter.

The Orion Crew Module (CM) is illustrated in Figure 2. The Orion CM is designed to carry up to four crew members, compared to a maximum of three in the smaller Apollo CM.

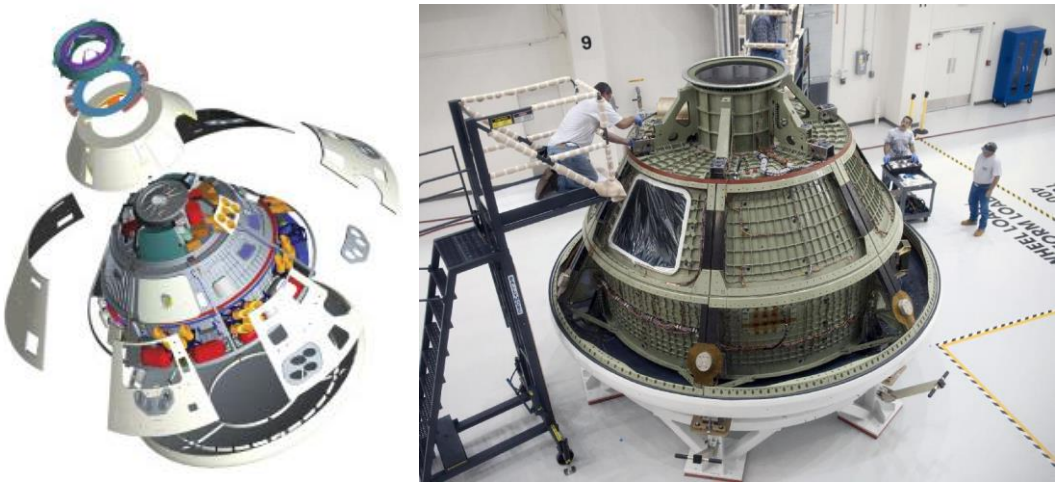

Figure 2. Orion Crew Module (CM). (Left) exploded view. (Right) As fabricated Orion Ground Test Vehicle (GTV) with baseline composite HSC structure attached.

2.2 Heat Shield Carrier Structure

The HSC structure designed by the NESC team is illustrated in Figure 3. The HSC structure must hold the 5-meter (196.9 in) diameter Avcoat ablative thermal protection system (TPS) securely to the Orion CM.

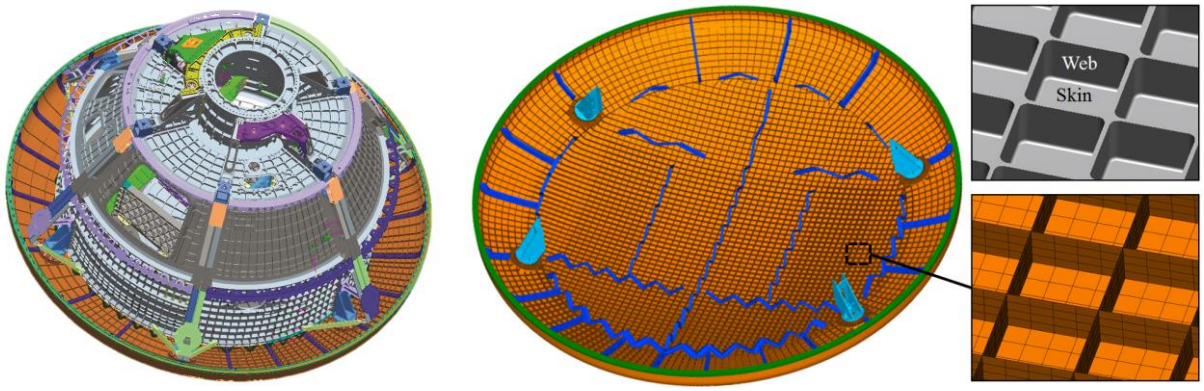

Figure 3. (Left) HSC structure interface to the Orion CM. (Right) NESC-developed orthogrid HSC design. Orthogrid skin and webs belonging to a single pocket are shown.

The HSC designed by the NESC team is a machined orthogrid concept. The carrier structure includes truss members and CM-SM retention and release (R&R) fittings for interfacing the heat shield assembly to the crew module. It was determined by the NESC that the orthogrid structure is especially suitable for a HSC application where the structure experiences aerodynamic and harsh landing loads which put the large panel bays into bending. Due to the increased bending stiffness provided by the orthogrid stiffening concept, this design was found to be lighter weight and more damage tolerant than unstiffened structural concepts (including the baseline design shown in Figure 20) with large, unsupported acreage skins.

2.3 Loading events

2.3.1 Reentry

Figure 4 includes a rendering of reentry in Earth's atmosphere returning from lunar orbit and the mechanical forces exerted on the HSC during this event.

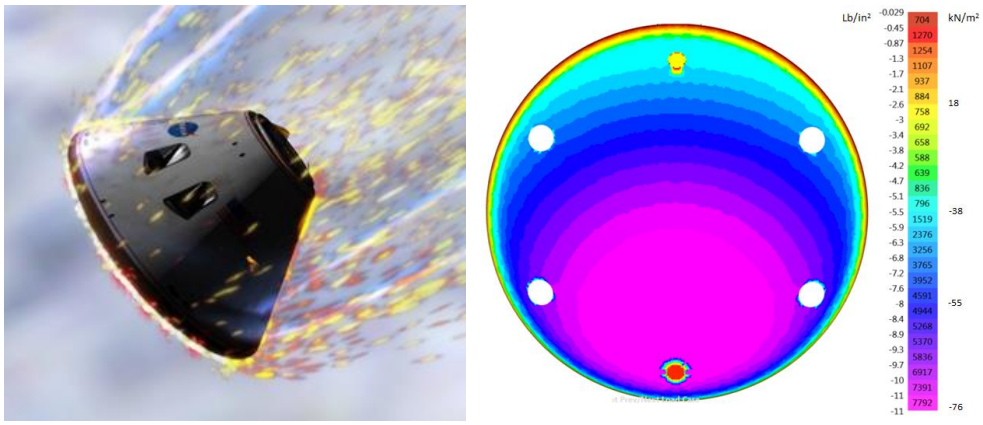

Figure 4. (Left) CM Earth reentry simulation. (Right) aerodynamic reentry pressure. Maximum pressure during a lunar-mission Earth reentry is approximately 76 Gpa (11 psi).

The Orion capsule re-enters the Earth atmosphere at speeds exceeding 11 kilometers per second (Mach 32.3). Due to the long duration of reentry it is treated as a static loading event.

2.3.2 Water Landing

The water landing loads are far more severe than the loads experienced during reentry. Reentry pressures on the outer skin peak at about 76 Gpa (11 psi), while landing loads peak well over 1300 GPa (200 psi). However, the peak pressures during landing are more localized and occur much faster than reentry. Figure 5 shows the capsule entering the water during a high-velocity water landing test at NASA Langley Research Center's Hydro Impact Basin. Figure 6 illustrates three discrete time steps from the landing simulation which captures the wave of high pressure moving over the heat shield as the capsule settles down to rest in a stable floating position.

Figure 5. Orion boilerplate test article (BTA) splashing down in Langley's Hydro Basin.

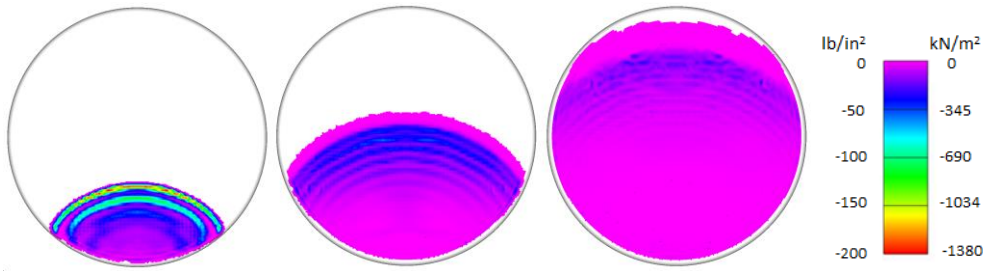

Figure 6. Landing simulation of the water pressure wave traveling across carrier structure. The uncolored regions have yet to make contact with water.

The water landing is a dynamic loading event that takes place very rapidly. The maximum forces imparted by the water to the crew module peak and dissipate in less than 50 milliseconds. This rapid pressure application produces inertial loads that require transient, non-linear FE analysis to properly capture accurate internal stress resultants. The landing simulations were run in LS-DYNA, a nonlinear transient explicit FEA solver. Each simulation introduces the complete vehicle to a water pool with various speeds and orientations for the mix of re-entry and launch abort cases with varying impact velocities.

2.4 Selected Material System

Ti-6Al-4V was selected as the material system for the orthogrid. The temperature knockdowns and Ramberg-Osgood parameters are referenced in MMPDS-06. The AMS 4920 F_{tu}/Fty specification of 896/827 MPa (130/120 ksi) allowables are reduced to appropriate knocked-down design allowables. Discussions with the forging supplier indicated only the latter strengths could be guaranteed for the entire forging. One of the factors for the selection of a metallic material is the non-linear strength and plastic bending capability at ultimate applied load, discussed in section 4.

3. SIZING

HyperSizer software was used with linear and non-linear FEA solvers (Nastran and LS-DYNA) as the sizing and optimization software tool for the NESC HSC structure. The HyperSizer sizing approach is based on detailed and accurate analysis methods that include the complete set of potential failure modes required for final design and margin of safety reporting. See section 4 for a listing of failure analysis used to size the titanium heat shield carrier structure. The integrated FEA-HyperSizer sizing approach was used throughout the life of the program, from preliminary sizing to detailed sizing and final analysis.

3.1 Preliminary Sizing

For preliminary sizing, smeared models were used to determine the optimum orthogrid configuration. In smeared models, panel candidates are evaluated using equivalent stiffness methods that do not require explicit stiffening features in the finite element model. The internal load path was computed using linear and nonlinear, transient FEA solvers (Nastran and LS-DYNA). The dimensions such as orthogrid web height and spacing, are represented using homogenization, or "smearing", techniques intrinsic in the HyperSizer sizing software [1]. The distinction between orthogrid skins and webs is shown in Figure 3. The primary advantage of the smeared approach is changes to the FE mesh are not required to investigate different web spacing and height configurations and grid patterns. Figure 7 shows the component definition of the smeared orthogrid FE model and the resulting orthogrid web spacing and web height trends computed using the smeared FE model.

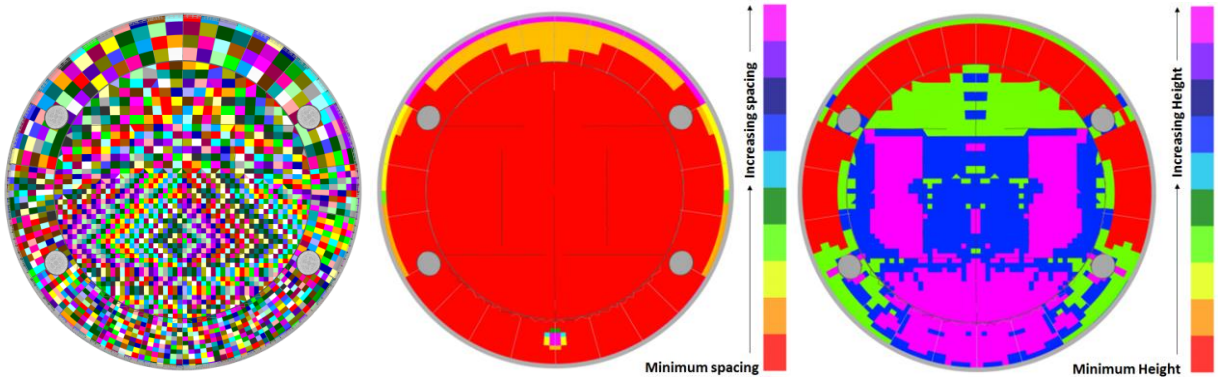

Figure 7. Smeared model used for preliminary sizing. (Left) sizing component definition, (middle) optimum web spacing trend, (right) optimum orthogrid total height trend.

The orthogrid web spacing was driven to a minimum allowed spacing everywhere by the snap-through buckling requirement during reentry (see section 4.1). The total orthogrid height was driven by global buckling requirements. The minimum spacing and maximum height restrictions were set based on discussions with the HSC manufacturing team.

3.2 Detailed Sizing

Detailed sizing of the Titanium orthogrid HSC structure was performed with an explicit FE model. The explicit FE model was created based on the optimum dimensions derived from the smeared sizing approach described in section 3.1. The process and analysis tools used to perform the detailed sizing and analysis are described in Figure 8.

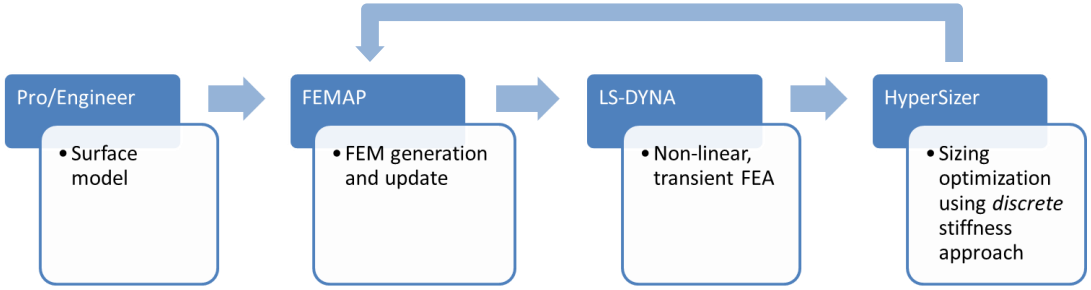

Figure 8. Detailed sizing approach using commercial software tools

The explicit surface model was created in ProEngineer. The FE mesh was created in FEMAP in Nastran format and then translated to LS-DYNA format. Simulations of the landing events were run with LS-DYNA. Due to the extended processing time, only a limited number of dynamic landing events thought to be the most severe were executed in LS-DYNA. The resulting element forces from each time step are translated from LS-DYNA output binaries into OP2 files and imported into HyperSizer for detailed sizing. After sizing, HyperSizer updated the gage thickness dimensions of the orthogrid webs/skins in the Nastran FE model. Revisions to the LS-DYNA model required manual updates to the input LS-DYNA file. At this point, LS-DYNA is re-executed to recalculate the internal loads which were then fed back into HyperSizer for another round of detailed sizing. This iterative process was repeated until the titanium HSC design showed positive margin and analytically demonstrated no buckling at ultimate loads, and no detrimental yield at limit loads. The resulting element forces from the final iteration are imported back into HyperSizer for reporting final margins of safety for the resulting gage thicknesses. Figure 9 shows the final gage thicknesses for the orthogrid skin and webs.

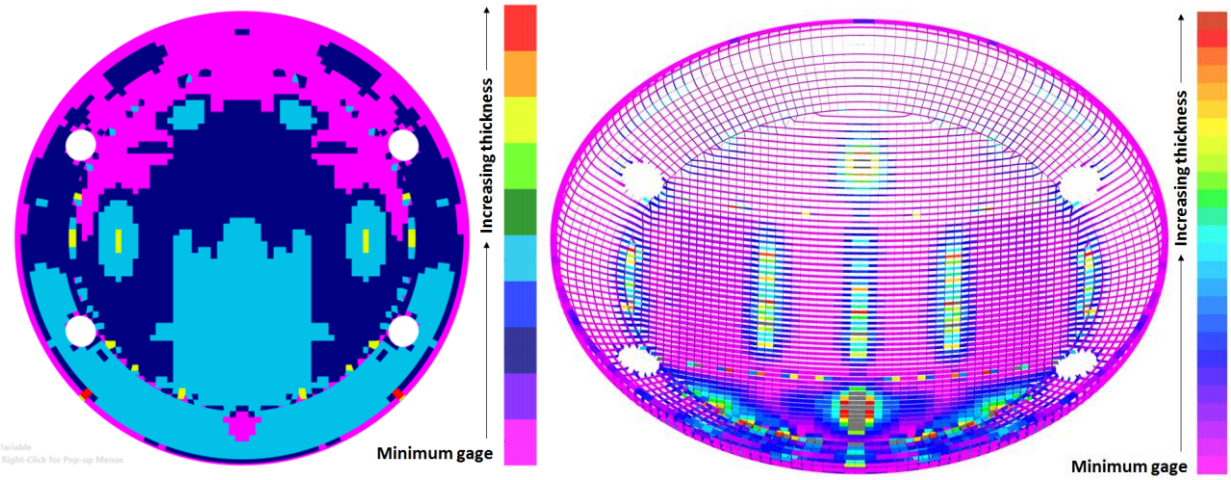

Figure 9. Explicit model used for detailed sizing. (Left) skin pocket gage thickness trend, (right) orthogrid web gage thickness trend, webs with thickness greater than 8mm (0.32 inch) displayed in grey.

The orthogrid skin pocket thickness was driven primarily by the snap-through buckling requirement on reentry, described in section 4.1. The web gage thickness was driven by the strength and stability methods described in sections 4.2 and 4.3. Notice the orthogrid web thickness increases at the orthogrid web to truss interfaces. The load introduction in the orthogrid webs is such that the web outer fiber experiences high compression loading which causes the gage thickness of the webs to increase to provide local strength and buckling stability.

4. ANALYSIS METHODS

Collier Research Corp. and SDA developed analytical methods to assess the strength and stability of the titanium HSC structure. The failure methods identified as critical for the heat shield carrier structure were implemented in HyperSizer as custom analysis plugins [2]. These failure methods are listed in Table 1.

Table 1. Custom failure analysis developed for sizing/analysis of the Titanium Orthogrid Heat Shield Carrier Structure

Mode	Component(s)	Comments
Snap-Through Buckling	Orthogrid Skin	• Stability margin written against applied external pressure • Doubly curved plate with fixed support on all edges • Stiffness of ablative Avcoat TPS ignored
Local Buckling	Web Segments	• Plate with SSSF boundary conditions • Accounts for compression and in plane bending loads • Includes plasticity reduction factor • Outer-fiber stress calculated from equivalent beam forces
Ultimate Strength	Web Segments	• Interaction equation based on cross sectional force and moments • Plastic bending • Assumes trapezoidal stress distribution past yield

4.1 Snap-Through Buckling of Orthogrid Skin

The heat shield orthogrid pocket skins are doubly curved shells (spherical shape) originally assumed to be simply supported by the webs and loaded by external pressure, as shown in Figure 10.

Figure 10. Reentry pressure load on orthogrid skin pockets.

Consider the curved panel under uniform radial pressure, q with pinned infinite edges A and B. A closed form solution for the critical pressure at which snap-through buckling is initiated (q') is found in Roark [3].

$$q' = \frac{Et^3\left(\frac{\pi^2}{\alpha^2} - 1\right)}{12r^3(1-v^2)} \qquad \alpha = \frac{AB}{2r} \tag{1}$$

A structural requirement for the orthogrid skins is the skin pockets are not permitted to snap-through during reentry. Large elastic deformations of the orthogrid skin put the Avcoat TPS at risk of cracking during reentry. Landing loads are treated differently. Since the TPS is merely treated as parasitic mass during landing, large deflection modes (including snap-through buckling) are permitted. This is an important distinction which led the NESC team to analyze the orthogrid skin pockets assuming the local orthogrid skin pockets react the high landing pressures in membrane. Nonlinear analysis verified the orthogrid skins could easy withstand the severe landing pressures in membrane through plastic deformation. This left the sizing of the orthogrid skin and orthogrid web spacing dimensions to be driven by the snap-through buckling requirement for reentry pressures.

4.1.1 Verification with Non-Linear FEA

Non-linear Nastran FE models were used to verify the analytical snap-though buckling method described in section 4.1. An example of one such FE model is shown in Figure 11.

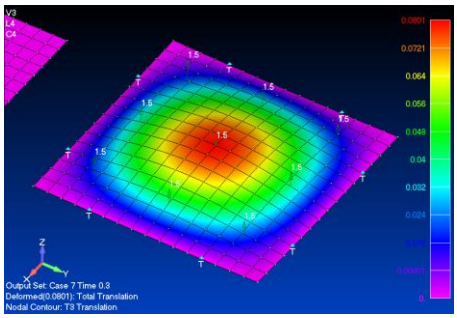

Figure 11. Nastran verification FE model. Doubly curved surface with slight curvature. Edges are pinned and a single pressure is applied inward on OML face normal to element surface.

First, a large 9in span was investigated. By plotting the center node displacement pocket snap through was evident between 2.8 and 3.1 GPa (0.41 and 0.45 psi). This agrees very well with the

analytical prediction of 2.82 GPa (0.41 psi). A comparison of the analytical and numerical snap-through buckling analysis for the 9in span doubly curved plate is shown in Figure 12.

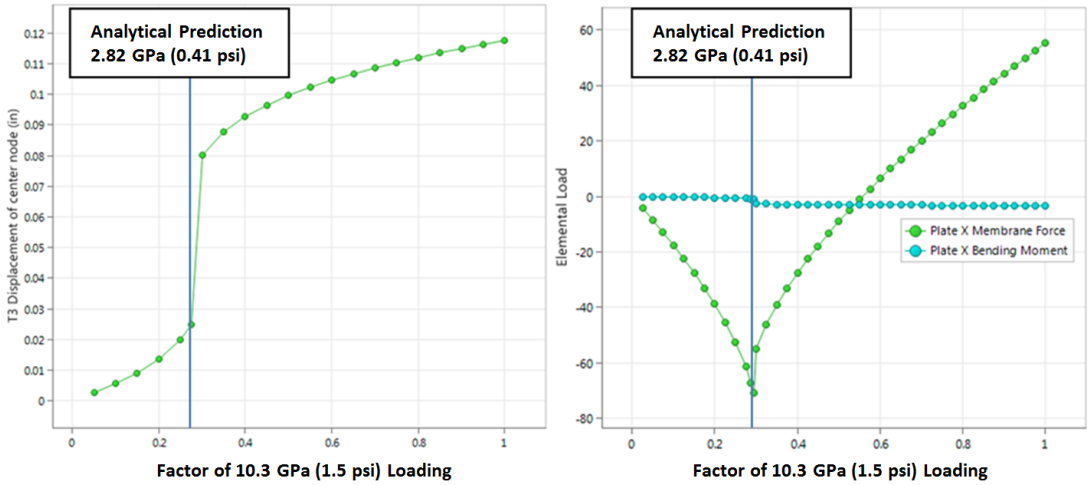

Figure 12. Displacement vs. load curve (left) and element load vs external load curves (right) for a 228.6mmx 228.6mm x 1.27mm (9" x 9" x 0.05") pocket with pinned edges

As the load on the plate increases, the spherical shape of the pocket skin reacts the inward pressure through compression only up to a point as predicted by the analytical and numerical buckling methods. After the snap-through event the element membrane forces become increasingly positive as the applied pressure increases.

For sizing the titanium orthogrid skin, the Roark formula was used with a fixed boundary factor to size orthogrid pockets from ultimate reentry pressures. Fixed supports by the skin-web interface were assumed since the analysis was leaning towards small pockets, 63.5mm x 63.5mm (2.5" x 2.5"), with short edge distances and a manufacturing requirement of 6.35mm (¼") fillets. A comparison of the analytical and numerical analysis for varying pocket size is shown in Figure 13.

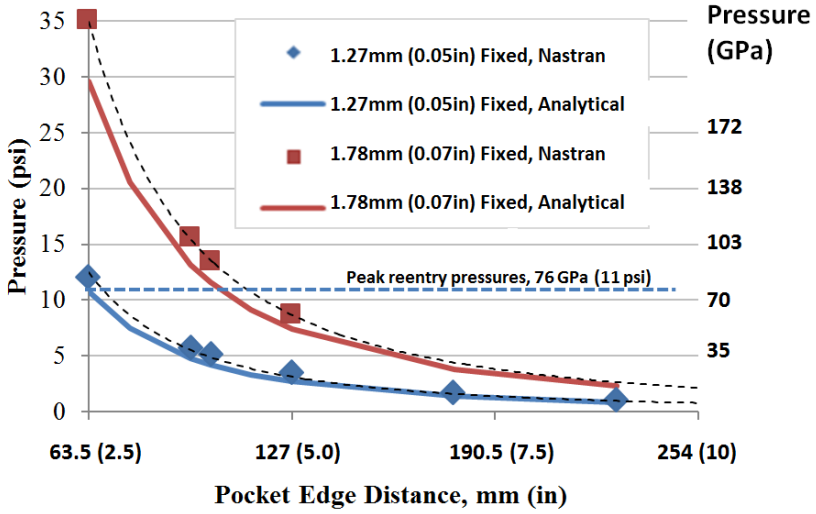

Figure 13. Critical buckling pressures as predicted by Roark and Nastran for different sized plates with fixed edges.

By studying Figure 13, we observe the analytical predictions are conservative when compared to the numerical analysis.

4.2 Strength Analysis of the orthogrid webs

For the ultimate strength analysis of the orthogrid web segments, a load processing method was developed with the intention to write margins of safety based on equivalent beam forces in each orthogrid web segment. The approach illustrated in Figure 14 requires unique reserve factors be written for axial and bending loads. A quadratic interaction is used to write margins of safety for the combined compression-bending load state.

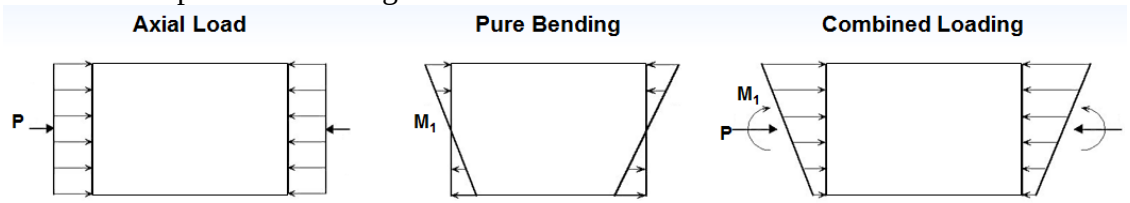

Figure 14. Equivalent beam forces extracted for orthogrid webs and truss flange segments

The reserve factor for axial load is calculated based on the material yield stress allowable. For bending, a perfectly-plastic beam assumption is used to calculate the resisting moment. The resisting moment is the moment required to cause the web to respond perfectly plastic. This moment is calculated based on the following relationship:

$$M = t\sigma_{yp}\left(h^2 - \frac{e^2}{3}\right) \quad [2]$$

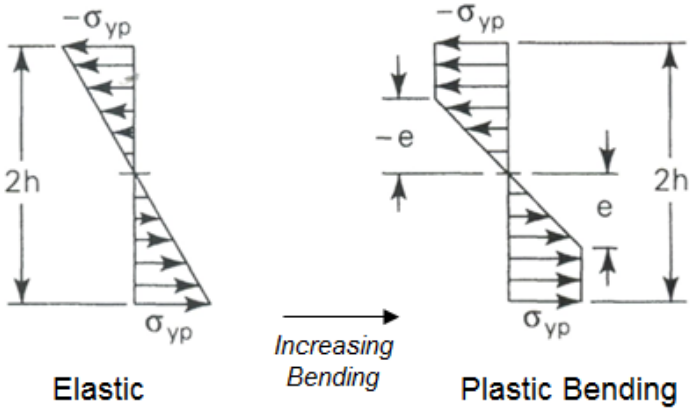

Figure 15. Bending stress distribution in a rectangular beam with increasing bending moment (left) elastic, (right) partially plastic [3].

When e = 0, the segment is totally plastic and Mp is the bending moment at which the segment is fully plastic.

$$M_p = th^2\sigma_{yp} \quad [3]$$

Where σ_{yp} is the material yield stress .For compression analysis, the resisting moment is assumed to be the moment that causes the web to go perfectly plastic. For tension analysis a trapezoidal stress distribution is assumed to capture the plastic behavior of the web past yielding. So the

resisting moment is determined from the superposition of the plastic bending moment and the additional moment required to drive the outer-fiber to ultimate tensile stress allowable.

$$M_r = th^2\sigma_{yp} + \frac{1}{6}bh^2(\sigma_u - \sigma_{yp}) \quad [4]$$

In most cases, the additional moment is a relatively small improvement to the resisting moment as it accounts for less than 5% of the total resisting moment.

4.3 Buckling Stability of the Orthogrid Web Segments

The local buckling behavior of orthogrid web segments is evaluated based on buckling for flat plates with linearly varying edge loading in the x-direction, illustrated in Figure 16

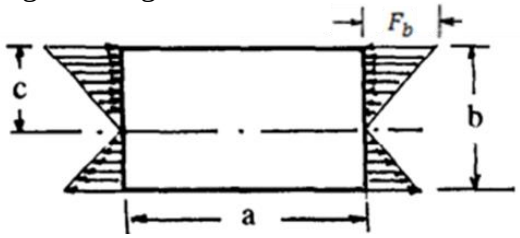

Figure 16. Flat Plate with linearly varying edge loads caused by in plane bending

Two methods are combined to capture the buckling eigenvalue for plates with in-plane moments causing linearly varying plane stress. The first method includes orthotropic stiffness terms so it is applicable for composite plates and stiffened panels with varying D_{ij} stiffness terms [4]. The initial buckling stress (at extreme fiber) is computed for an orthotropic plate with SSSS constraints in pure bending ($\alpha = \frac{b}{c} = 2$)

$$F_b = k_0 \frac{\pi^2\sqrt{D_{11}D_{22}}}{b^2 t} \quad [5]$$

Design curves, found in Leissa [4], list the buckling coefficient, k_0 with respect to the stiffness parameter. For isotropic plates the stiffness parameter is 1.0, and equation [5] simplifies to:

$$F_b = K_b \eta_c E \left(\frac{t}{b}\right)^2 \quad [6]$$

Where η_c is the plasticity reduction factor (derived from Ramberg-Osgood parameters found in MMPDS) for compression stress.

$$\eta_c = \sqrt{\frac{1}{1 + \left(\frac{0.002\ E\ n}{F_{cy}}\right)\left(\frac{F_c}{F_{cy}}\right)^{n-1}}} \quad [7]$$

K_b for a plate in pure bending and SSSS boundary conditions is

$$K_b = \frac{k_0\pi^2}{12(1-v^2)} \quad [8]$$

Design curves, found in Niu [5], list bending bucking coefficients (K_b) for varying edge boundary conditions and bending ratios.

Combining the methods into a single governing equation yields a method that accounts for varying the orthotropic Dij stiffness, bending ratios and buckling boundary conditions. The combined equation is written in the form:

$$F_b = \eta_c k_0 \frac{\pi^2 \sqrt{D_{11} D_{22}}}{b^2 t} \frac{K_{b(desired\ bc)}}{K_{b\ (\mathrm{SSSS})\ \alpha = 2}} \quad [9]$$

A more rigorous derivation of the method will be published as part of the NESC heat shield final report.

4.3.1 Impact of Segment Aspect Ratio

The design curves presented in Niu [5] assume the plates have infinite aspect ratio. As a result the analytical method returns an equivalent critical buckling stress regardless of the length of the plate. To quantify the effect of the aspect ratio, FEA verification of the pure bending, plate buckling analysis method was performed with 21 data points representing a range of aspect ratios and boundary conditions, summarized in Figure 17. The failure ratio for each set of boundary conditions is determined as a function of segment aspect ratio. The failure ratio is defined as the FEA buckling load divided by the analytical buckling load. A failure ratio greater than one indicates a conservative comparison since the FEA-computed failure load exceeds the analytical prediction.

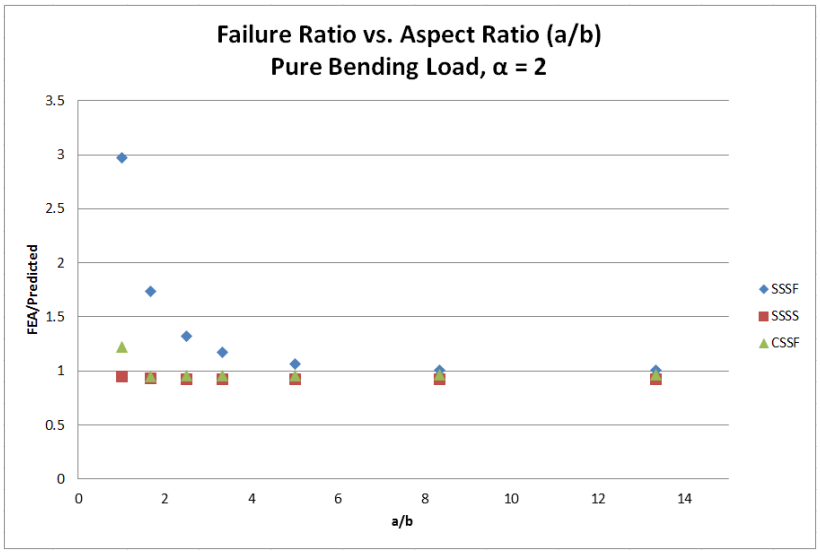

Figure 17, Failure ratio (FEA/Predicted) with respect to panel aspect ratio.

By studying Figure 17, we observe the analytical method matches the FEA results for SSSS and CSSF conditions for aspect ratios greater than one. However, for plates with SSSF boundary conditions the analytical method is over-conservative for segments with low aspect ratios. Furthermore, the plates with SSSF edge conditions appear to be more sensitive to the length of the unsupported edge.

By studying the buckling mode shapes, shown in Figures 18 and 19, we observe the plate with SSSF boundary conditions (Figure 18) only ever has one half mode shape, for aspect ratios

ranging between 1.5 and 5. On the other hand, the web segments with CSSF boundary conditions (Figure 19) switch to multiple half mode shapes as the aspect ratio increases, which makes the buckling modes less sensitive to increasing aspect ratio.

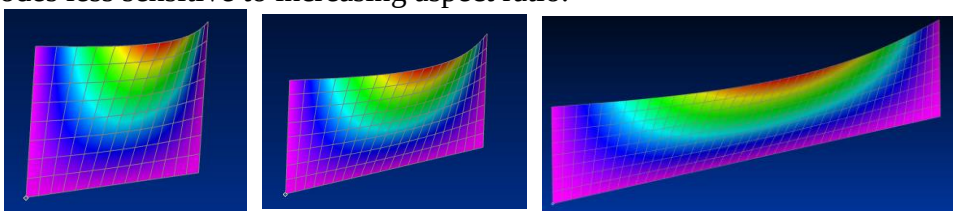

Figure 18, Buckling mode shapes for segments with in plane bending and **SSSF** boundary conditions. (Left) a/b = 1.5, (middle) a/b = 2.5, (right) a/b = 5.

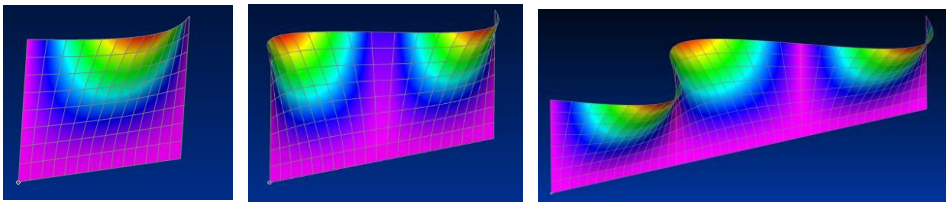

Figure 19, Buckling mode shapes for segments with in plane bending and **CSSF** boundary conditions. (Left) a/b = 1.5, (middle) a/b = 2.5, (right) a/b = 5.

In summary, an additional FEA-derived buckling coefficient is required to reduce the conservatism of the analytical method for plates with SSSF conditions with low aspect ratios.

The critical shear buckling stress is calculated for flat plates with uniform shear loading using curves from NASA TN D-8257 [6]. The method is valid for varying aspect ratios. Design curves are required to define the shear buckling coefficients for plates with various boundary conditions [5]. Interaction equations for combined compression, bending and shear were used.

5. TRADE STUDIES

5.1 Structural Architectures

Early on in the design two competing structural architectures were being considered. Conceptual trade studies were performed to assess the structural efficiency of two primary architectures illustrated in Figure 20.

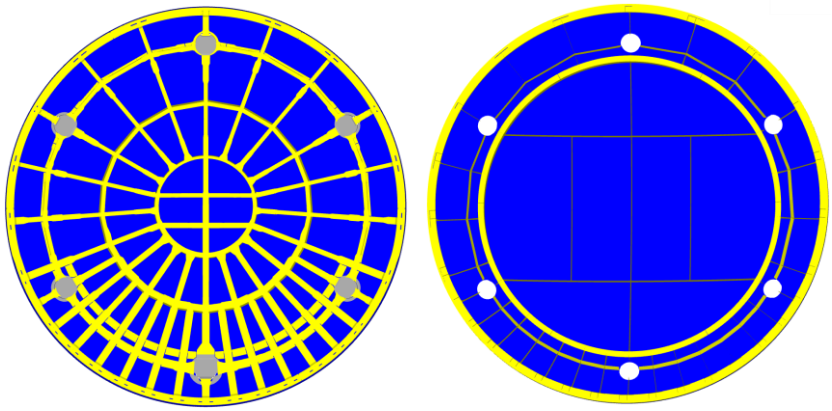

Figure 20. HSC architectures. (Left) "Wagon wheel" configuration, (right) "Load sharing" configuration.

The original design was a skin-stringer design referenced to as the "wagon wheel". Numerous skin material and structural concepts were evaluated using the wagon wheel architecture, see Table 2.

5.1.1 Wagon Wheel Weight Trades

Table 2. HSC structural concepts, wagon wheel architecture. FEM mass reported in Figure 21.

Concept	Material (skin)	Skin Panel Concept	Material (stringer)
1	T300 Fabric	Quasi-isotropic Laminate	Ti-6Al-4V
2	T300 Fabric	Tailored Laminate	Ti-6Al-4V
3	Ti-6Al-4V	Unstiffened Plate	Ti-6Al-4V
4	13-8 Mo Stainless	Unstiffened Plate	13-8 Mo Stainless
5	Al-2219	Unstiffened Plate	Al-2219
6	T300 Fabric	Honeycomb Sandwich Quasi skins	Ti-6Al-4V
7	T300 Fabric	Honeycomb Sandwich tailored skins	Ti-6Al-4V
8	Ti-6Al-4V	Blade stiffened (H≤2.5)	Ti-6Al-4V
9	Ti-6Al-4V	Blade stiffened (H≤2)	Ti-6Al-4V
10	Ti-6Al-4V	I Stiffened	Ti-6Al-4V
11	Ti-6Al-4V	Orthogrid	Ti-6Al-4V
12	13-8 Mo Stainless	Orthogrid	13-8 Mo Stainless
13	13-8 Mo Stainless	Orthogrid	Ti-6Al-4V

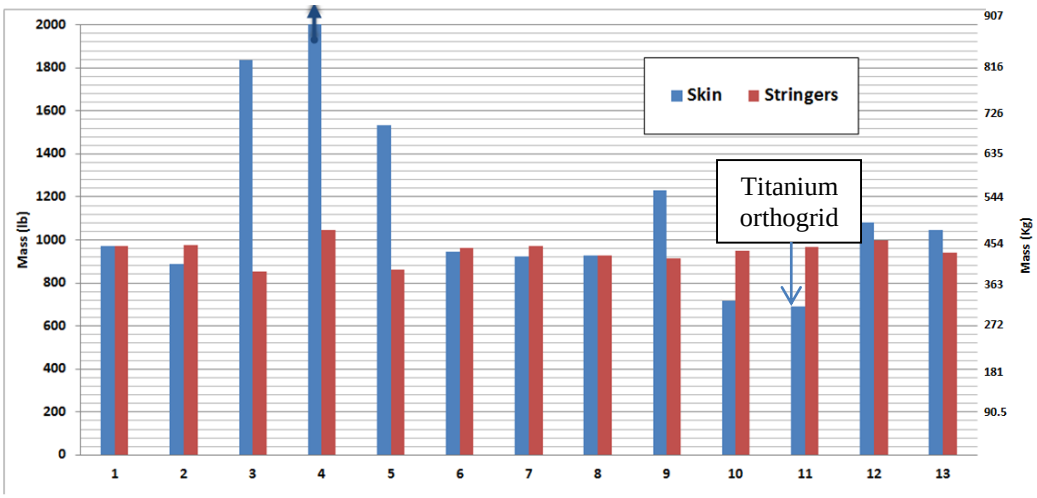

Figure 21. FEM mass comparison of the various stiffening concepts and material systems evaluated for the wagon wheel architecture. Description of concept listed in Table 2.

5.1.2 Load Sharing Weight Trades

After studying the “wagon wheel" design, the NESC assessment team began developing an alternative concept that took advantage of "load sharing" with the crew module backbone, replaced the existing wagon wheel stringer design with an H beam configuration.

Table 3. HSC structural concepts, load sharing architecture. FEM mass reported in Figure 22.

Concept	Material	Panel Concept
1	T300 Fabric	Composite Laminate
2	T300 Fabric	Honeycomb Sandwich
3	Ti-6Al-4V	Blade Stiffened
4	Ti-6Al-4V	Orthogrid

5	13-8 Mo Stainless Steel	Orthogrid
6	T300 Fabric	I Stiffened
7	T300 Fabric	T Stiffened

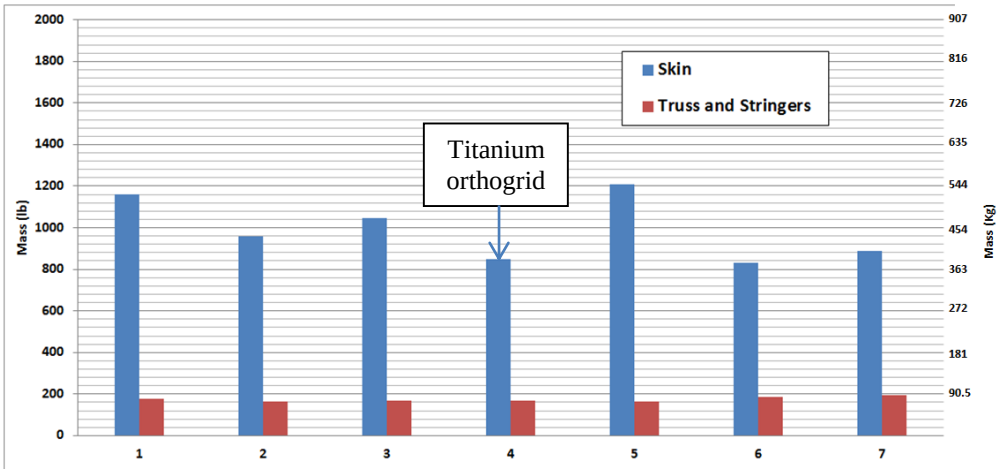

Figure 22. Mass comparison for all concepts investigated for load sharing structural architecture

Encouraged by weight savings realized by the alternate Titanium orthogrid load sharing design, in early February 2013, the NESC down-selected to the titanium orthogrid option. It should be noted that composite I and T stiffened concepts also showed promise. However, due to inherit complexities in manufacturing the composite skin-stringer designs were not selected.

6. CONCLUDING REMARKS

The NESC assessment team concluded that the titanium orthogrid is a valid structural concept for the CM HSC and it provides ample mass-saving opportunity over other HSC concepts investigated by the NESC. By taking advantage of the increased bending stiffness of the orthogrid stiffening concept and the plastic strain behavior of titanium, the NESC HSC design is a more attractive option than unstiffened HSC concepts with brittle material systems. It should be noted as design requirements changed as the program matured, the titanium orthogrid HSC structural mass did not increase. In fact, the orthogrid FEM mass estimated in the preliminary trade studies was within 5% of the FEM mass for the final design. This proves two things, (1) the robustness of the design/analysis process and (2) the adaptability of the orthogrid design to large-scale configuration changes and additional design requirements.

7. REFERENCES

1. Collier Research Corp., HyperSizer Methods and Equations, Thermo-elastic Stiffness Formulation, Oct 2011.
2. HyperSizer version 7.0 user documentation, About Analysis Plugins, 2014.
3. Ugural A. C, Advanced Strength and Applied Elasticity, 4th edition, 2003.
4. Leissa, A., Buckling of Laminated Composite Plates And Shell Panels. AFWAL-TR-85-3069 Air Force Flight Dynamics Laboratory, 1985.
5. Niu, M. C., Airframe Stress Analysis and Sizing. Conmilit Press Ltd., 1997.
6. Jefferson W., Agranoff N., Minimum-mass Design of Filamentary Composite Panels Under Combined Loads, NASA TN D-8257, LaRC Hampton VA, 1976.